Analysis of 3-D Metallization Structures by a Full-Wave Spectral Domain Technique

Thomas Becks, *Member, IEEE* and Ingo Wolff, *Fellow, IEEE*

Abstract—**A full-wave method for the investigation of microstrip- and coplanar-structures including 3-D metallization structures is presented. The spectral domain analysis method is used to calculate the *S*-parameters of unshielded microwave components containing bond-wires and air-bridges. The general formulation and the implementation procedure of the method are described. The application of the theory is given by a comparison of measured and calculated results for a spiral inductor, including an air-bridge.**

I. Introduction

BOND-WIRES, via-holes and air-bridges are indispensible to circuit design. They are used to ensure the biasing of active areas and to suppress multimode propagation along the RF signal paths. The introduction of new three-dimensional passive devices which yield higher package densities reducing size, weight and cost necessitate progress in analysis and circuit design. Most of the commercially available software for the characterization of passive structures is based on models, or can only handle planar structures in the sense of a full-wave analysis. Up to now, the full-wave analysis of such real three-dimensional structures could only be done using the finite-difference approach [1], [2] or the transmission line matrix method [3].

The spectral domain analysis (SDA) technique [4], [5] and the basically equivalent space-domain integral technique [6], [7] are well-known in the literature. These full-wave analysis methods use roof-top functions as expansion functions for the surface current density and have proven to be flexible tools for the calculation of arbitrary shaped planar passive microwave structures. Due to the implementation of an FFT-algorithm and iterative methods, efficient *S*-parameter calculations of complex planar circuits has become possible [8]. These methods can take into account effects of multilayer structures as well as losses due to surface waves, radiation and non-ideal strip and backside metallization (if existing). But in general, both methods only can handle structures with planar metallizations.

Recently, two hybrid methods [5], [6] have been introduced to overcome this major drawback of integral equation methods applied to coplanar structures. In [5], some 3-D geometries are handled by first generating an *S*-parameter representation of the planar structure. Afterwards the third dimension is included into the calculation by applying suitable air-bridge descriptions in the sense of a hybrid method. In a very similar approach in [6] the frequency equivalent circuit of the planar discontinuity without the air-bridge is derived using SDA method. Then, the circuit is modified by using a quasi-static lumped element model of the air-bridge. Both formulations are looking for the third dimension of the structure under consideration only in the sense of a segmentation approach. Air-bridges at internal ports cannot be included into the calculation procedure. In [9] the spectral domain method in connection with image theory is used to calculate 3-D coplanar structures. This approach can be used for coplanar circuits only.

In this paper, air-bridges and bond-wires are included in a full-wave analysis using the spectral domain technique to analyze microstrip structures. Electromagnetic effects due to electric currents in the horizontal and vertical directions are considered in the approach. This is done by formulating the dyadic Green's function for currents in the horizontal and vertical directions (Section II-A). For coplanar structures, magnetic planar surface current densities can be used to restore the electric fields in the slots. The dyadic function is formulated either for an open or shielded structure, so antenna problems can be handled very easily. Section II-B presents the description of horizontal and vertical directed parts of the bridge by surface currents or either a volume current formulation. After introduction of matched sources, an integral equation can be formulated and solved by the method of moments in connection with direct or iterative solutions for the resulting system of linear equations (Section II-C). Section II-D gives insight into the S-parameter extraction technique used here. In Section III, numerical results for the scattering parameters of microstrip discontinuities such as bonded gaps and rectangular spiral inductors are discussed and compared with available measurements and FDTD results.

II. Theory

Fig. 1 shows the geometry of a typical 3-D microstrip structure, a rectangular spiral inductor on a dielectric substrate backed by a metallization. The spiral inductor con-

Manuscript received July 10, 1992; revised July 30, 1992.

The authors are with the Department of Electrical Engineering, and Sonderforschungsbereich 254, Duisburg University, Bismarckstr. 81, D-4100, Duisburg 1, Germany.

IEEE Log Number 9203684.

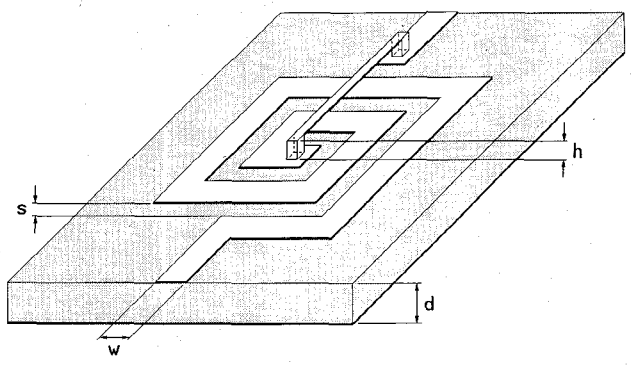

Fig. 1. Schematic view on a rectangular spiral inductor in microstrip technique.

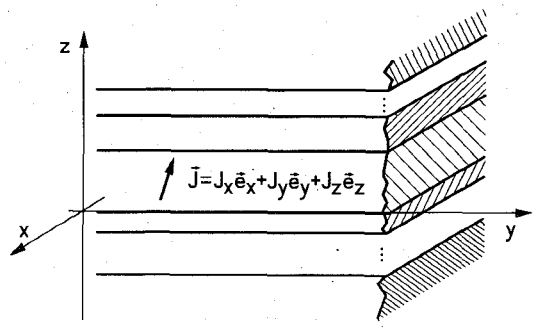

Fig. 2. Geometry of a generalized multilayer configuration of dielectric substrates.

tains two turns and a bond-wire or air-bridge connects the center with the outgoing port. The substrate is assumed infinitely wide in the x- and y-directions. The structure is unshielded.

A. The Dyadic Green's Function

The full-wave analysis of a microstrip discontinuity begins with the derivation of the Green's function of a Hertzian dipole in a layered medium (Fig. 2). In [10] an iterative algorithm has been developed to define electromagnetic fields due to a current element in the horizontal direction ($\boldsymbol{J} = \boldsymbol{J}_s = J_x \boldsymbol{e}_x + J_y \boldsymbol{e}_y$) inside a multilayered structure. An extension to vertically directed current elements ($\boldsymbol{J} = \boldsymbol{J}_s + J_z \boldsymbol{e}_z$) was introduced in [11]. Outside the source region, the field consists of a superposition of transverse electric (TE) and transverse magnetic (TM) waves with respect to the interface normals. Because of this fact, decomposing the field using the z-components of the electric and magnetic vector potential ($\boldsymbol{F}$ and $\boldsymbol{A}$) is useful to look for the problem as a transmission line problem in z-direction. Details of the derivation of the dyadic Green's function in the spectral domain (superscript $\tilde{}$) are given in the references [10], [11]. From the linearity of the problem it follows that the electric field $\boldsymbol{E}_i$ in each layer i excited by a current density $\boldsymbol{J}$ can be calculated as:

$$\boldsymbol{E}_i(x, y, z) = (4\pi^2)^{-1} \int_{z0} \int_{k_x} \int_{k_y} \tilde{\boldsymbol{G}}_{E_i,J}(k_x, k_y, z - z_0) \cdot \tilde{\boldsymbol{J}}(k_x, k_y, z_0)\, e^{-j(k_x x + k_y y)}\, dk_x\, dk_y\, dz_0. \quad (1)$$

Assuming a two layer case (Fig. 1), the first two columns of the dyadic Green's function for the area of interest $z > d$ are well-known. In addition the third column—$\tilde{\boldsymbol{E}}$-field excited by a vertical directed current—is given by

$$\tilde{G}_{E_u,J_z} = \frac{k_u}{2\omega\epsilon_2} \left[\frac{Q(k_x, k_y)}{T_m(k_x, k_y)}\, e^{j2\beta_2 d} e^{-j\beta_2(z + z_0)} + \operatorname{sign}(z - z_0)\, e^{-j\beta_2 |z - z_0|} \right], \quad (2)$$

and

$$\tilde{G}_{E_z,J_z} = -\frac{k_x^2 + k_y^2}{2\omega\epsilon_2\beta_2} \left[\frac{Q(k_x, k_y)}{T_m(k_x, k_y)}\, e^{j2\beta_2 d} e^{-j\beta_2(z + z_0)} + e^{-j\beta_2 |z - z_0|} \right] - \frac{\delta(z - z_0)}{j\omega\epsilon_2}, \quad (3)$$

where the following terms are defined:

$$Q(k_x, k_y) = k_0^2 \epsilon_r \beta_2 \cos(\beta_1 d) - j k_0^2 \beta_1 \sin(\beta_1 d) \quad (4)$$

$$T_m(k_x, k_y) = k_0^2 \epsilon_r \beta_2 \cos(\beta_1 d) + j k_0^2 \beta_1 \sin(\beta_1 d) \quad (5)$$

$$\beta_1^2 = k_0^2 \epsilon_r - k_x^2 - k_y^2 \quad (6)$$

$$\beta_2^2 = k_0^2 - k_x^2 - k_y^2 \quad (7)$$

and

$$u = x, y. \quad (8)$$

Physical phenomena like losses due to surface waves, radiation, and non-ideal dielectric materials are taken into account. Especially surface waves and radiation contribute to power loss for the structure under consideration. The zeros of T_m in the denominators of (2) and (3) correspond to the TM surface wave modes.

B. Current Expansion Functions

The next step of the procedure is to represent the currents on the metallization structure approximately by a set of expansion functions with unknown coefficients. The choice of current expansion functions can be divided into two parts:

(a) Horizontally directed parts of the metallization structure can be described approximately by surface current densities. After introducing a rectangular uniform mesh (Fig. 3), representation of the surface currents is done by a "rooftop" distribution. Rooftop functions give a piecewise linear approximation to the current in the direction of current flow and a step approximation lateral to the

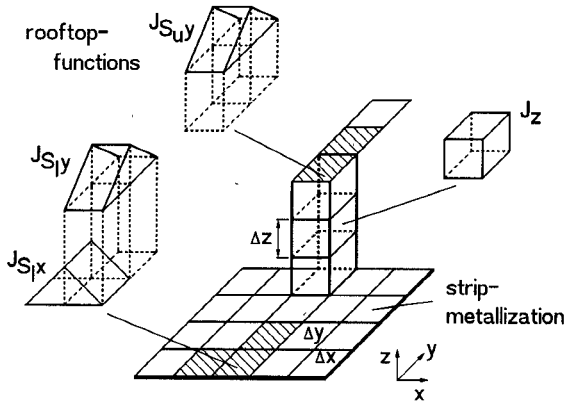

Fig. 3. Current-discretization procedure for a bond-wire structure with horizontal cross-sectional area equal to one cell.

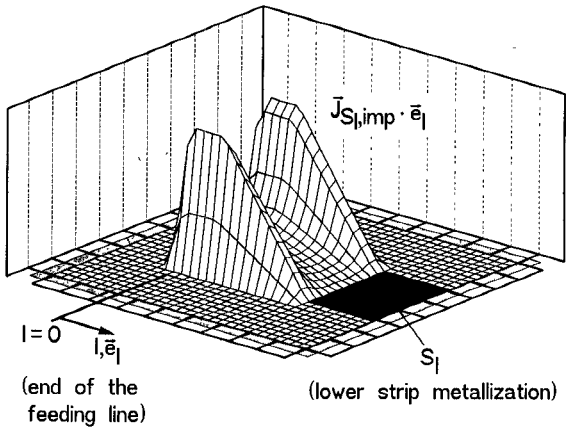

Fig. 4. Illustration of the placement and formulation of an impressed source current distribution $J_{S,imp}$. Located at the end of the feeding lines ($l = 0$) which are connected to the structure under consideration, the current distribution of the source is precomputed by solving an eigenvalue problem.

current flow. The mathematical expression of those rectangular subdomain functions is

$$J_{S,x}(m, n) = R\left(\frac{y - n\Delta y/2}{\Delta y}\right) T\left(\frac{x - m\Delta x}{\Delta x}\right) e_x, \tag{9}$$

where

$$R(y) = \begin{cases} 1, & |y| \le \dfrac{\Delta y}{2} \\ 0, & |y| > \dfrac{\Delta y}{2} \end{cases},$$

$$T(x) = \begin{cases} 1 - \dfrac{|x|}{\Delta x}, & |x| \le \Delta x \\ 0, & |x| > \Delta x \end{cases} \tag{10}$$

(y-directed current by interchanging m with n and Δx with Δy on the right hand side of (9)).

(b) Vertically directed parts of the metallization structure can be described approximately by volume current densities. As shown in Fig. 3, volume currents in the vertical direction represent a bond-wire structure with horizontal cross-sectional area equal to one cell. A local mesh refinement can be used to reduce the diameter of this part of the bridge. The mathematical expression for this step approximation is

$$J_z(m, n, i) = R\left(\frac{x - m\Delta x/2}{\Delta x}\right) R\left(\frac{y - n\Delta y/2}{\Delta y}\right) \cdot R\left(\frac{z - d - i\Delta z/2}{\Delta z}\right) e_z. \tag{11}$$

With the help of these two types of expansion functions provided above, the current distribution on any 3-D microstrip discontinuity can be expanded effectively. Even curved planar metallization structures can be handled by a staircase approximation [12]. Transmission lines connected to the structure under test are terminated by open-ends holding he current distributions of impressed sources (Fig. 4). So the entire region of interest has a finite dimension where only subdomain expansion functions are required. A special treatment of such open-end discontinuities introduced, is presented in the next sections.

C. The Integral Equation/Moment Method Solution

With (1), the electric field for $z > d$ is constructed from the unknown currents described above by replacing

$$\tilde{J}(k_x, k_y, z_0) = \tilde{J}_{S,l}(k_x, k_y)\,\delta(z_0 - d) + \tilde{J}_{S,u}(k_x, k_y)\,\delta(z_0 - d - h) + \tilde{J}_z(k_x, k_y, z_0), \tag{12}$$

with: subscript S_l = lower planar, subscript S_u = upper planar, and subscript z = vertically directed part of the metallization. Introduction of matched sources [13] at the ends of the lines feeding the structure under test lead to an excitation problem. By choosing the impressed source distributions $J_{S,imp}$ in modal form, the continuity of the current density from the sources to the feed lines is ensured with a minimum of disturbance. From the surface current point of view the end of the line looks like a matched load. The information about the current distribution of a single mode is precomputed by the analysis of the undisturbed lines as an eigenvalue problem. Fig. 4 illustrates the placement and the formulation of such current-matched sources by depicting the longitudinally directed part of the impressed current distribution.

A reaction J_{reac} of the system has to compensate the portion of the source field tangential to the planar, horizontally directed part of the metallization. In addition, the total electric field within the vertically directed parts of the metallization must be zero. In connection with (1) and (12), a Fredholm integral equation of the first kind results

$$E_{S_l}(J) + E_{S_u}(J) + E_z(J) = o, \tag{13}$$

where

$$\boldsymbol{J} = \boldsymbol{J}_{S_l,imp} + \boldsymbol{J}_{S_l,reac} + \boldsymbol{J}_{S_u,reac} + \boldsymbol{J}_{z,reac} \tag{14}$$

with S indicating planar metallization and z indicating vertical directed parts again.

The next step is the discretization of the electric fields tangential to or in the metallization in the sense of the well-known Galerkin procedure. This step projects the Fredholm integral equation ((13)) onto a system of linear equations

$$\begin{bmatrix} \boldsymbol{Z}_{S_l,S_l} & \boldsymbol{Z}_{S_l,S_u} & \boldsymbol{Z}_{S_l,z} \\ \boldsymbol{Z}_{S_u,S_l} & \boldsymbol{Z}_{S_u,S_u} & \boldsymbol{Z}_{S_u,z} \\ \boldsymbol{Z}_{z,S_l} & \boldsymbol{Z}_{z,S_u} & \boldsymbol{Z}_{z,z} \end{bmatrix} \begin{bmatrix} \boldsymbol{J}_{S_l} \\ \boldsymbol{J}_{S_u} \\ \boldsymbol{J}_z \end{bmatrix} = \begin{bmatrix} \boldsymbol{V}_{S_l,S_l,imp} \\ \boldsymbol{V}_{S_u,S_l,imp} \\ \boldsymbol{V}_{z,S_l,imp} \end{bmatrix}. \tag{15}$$

Each submatrix in the equation above represents a set of mutual impedances between expansion functions and testing functions. For example, a typical matrix element of the $\boldsymbol{Z}_{S_l,S_l}$-matrix looks like

$$Z^{x,x}_{S_l,S_l} = \left(\frac{4}{\pi\Delta x}\right)^2 \int_{k_x}\int_{k_y} \tilde{G}_{E_x,J_x}(k_x, k_y, d) \cdot \left[\frac{1}{k_x}\sin\left(k_x\frac{\Delta x}{2}\right)\right]^4 \left[\frac{1}{k_y}\sin\left(k_y\frac{\Delta y}{2}\right)\right]^2 \times e^{jk_x(m-M)\Delta x} e^{jk_y(n-N)\Delta y}\, dk_x\, dk_y. \tag{16}$$

From (16), it is evident that all $\boldsymbol{Z}$-matrix elements can be calculated by a 2D backward Fourier transform. Any submatrix in (15) can be performed efficiently by application of FFT techniques. In order to get correct results by using FFT, two facts have to be taken into account:

(a) The Nyquist theorem $k_{u,\max} \geq 2\pi/\Delta u$, $u = x, y$ must be fulfilled.
(b) A fine sampling rate around the poles of the Green's function and within an area $k_x^2 + k_y^2 \leq k_0^2$ must be chosen, in order to get the influences of surface waves and radiation into the calculation.

Because of these facts, FFT-dimensions could become large. To overcome these disadvantages, two different ideas have been used:

a) No sampling points have been located near to the poles. The interpolation or the translation theorem has been used.
b) Surface wave effects have been included by using residue theory around the poles to get additional parts to the "FFT" integral.

After performing a solution of the linear system with iterative methods like the conjugate gradient method [14] or the Lanczos algorithm [15], which is better suited to handle multiport problems, one can obtain the coefficients in $\boldsymbol{J}_{S_l}$, $\boldsymbol{J}_{S_u}$, and $\boldsymbol{J}_z$. The most time consuming part of an iterative algorithm is the matrix-vector-multiplication needed once or twice each iteration step. The $\boldsymbol{Z}_{S_l,S_l}$-matrix in eq. (15) contains four submatrices, each of block-Toeplitz type, Toeplitz submatrices within. Because of this fact, the main part of the matrix-vector-multiplication $\boldsymbol{Z}\hat{\boldsymbol{J}}$ can be handled as a convolution. Therefore an efficient usage of 2-D FFT algorithm becomes possible again [16].

D. S-Parameter Extraction

Efficient identification of discontinuity parameters is important to reduce the numerical effort for analyzing complex structures. The S-parameter extraction technique used here is similar to a method described in [1] for the calculation of generalized scattering parameters with a finite-difference method.

On an infinitely long, longitudinally homogeneous transmission line, in each cross-sectional plane the transverse electromagnetic fields can be described as a superposition of line modes. In a mathematical sense these modes form a complete set of functions,

$$\boldsymbol{E}^{\text{line}}_{tr}(u, v, l) = \sum_{\nu=1}^{M} \boldsymbol{t}^{\nu}_{E}\sqrt{Z^{\nu}_{F}}\,[a^{\nu}e^{-\gamma^{\nu}l} + b^{\nu}e^{\gamma^{\nu}l}] \tag{17}$$

$$\boldsymbol{H}^{\text{line}}_{tr}(u, v, l) = \sum_{\nu=1}^{M} \boldsymbol{t}^{\nu}_{H}(\sqrt{Z^{\nu}_{F}})^{-1}[a^{\nu}e^{-\gamma^{\nu}l} - b^{\nu}e^{\gamma^{\nu}l}], \tag{18}$$

with: $\boldsymbol{t}^{\nu}_{E}$, $\boldsymbol{t}^{\nu}_{H}$ the transverse vector functions of the transverse coordinates u and v, γ^{ν} the propagation constant, and Z^{ν}_{F} the wave impedance of the ν-th mode of the line. a^{ν} and b^{ν} are the amplitude coefficients of the ν-th forward and backward travelling line mode, respectively.

Fig. 5 shows a schematic view on an N-port structure under test. Each port is connected to a line and fed by a current source. In order to look for the generalized scattering parameters of the structure, reference planes at $l_{r,i}$ and "test" planes at $l_{t,i}$ are introduced (i = number of port, connected line). After introduction of impressed current source distributions, (15) can be solved for the unknown current amplitude coefficients. With the knowledge of the current distribution within the structure, the electromagnetic fields all over the space can be calculated. Especially the resulting transversal electromagnetic fields in the cross-sectional planes at $l_{t,i}$ (Fig. 5) are determined. Each of these transverse electromagnetic fields can be expressed as shown in (17) and (18)

$$\boldsymbol{E}^{n}_{tr,i}(u, v, l_{t,i}) = \sum_{\nu=1}^{M_i} \boldsymbol{t}^{\nu}_{E,i}\sqrt{Z^{\nu}_{F,i}}\,[a^{\nu,n}_{i}e^{-\gamma^{\nu}_{i}(l_{t,i}-l_{r,i})} + b^{\nu,n}_{i}e^{\gamma^{\nu}_{i}(l_{t,i}-l_{r,i})}], \tag{19}$$

$$\boldsymbol{H}^{n}_{tr,i}(u, v, l_{t,i}) = \sum_{\nu=1}^{M_i} \boldsymbol{t}^{\nu}_{H,i}(\sqrt{Z^{\nu}_{F,i}})^{-1}[a^{\nu,n}_{i}e^{-\gamma^{\nu}_{i}(l_{t,i}-l_{r,i})} - b^{\nu,n}_{i}e^{\gamma^{\nu}_{i}(l_{t,i}-l_{r,i})}], \tag{20}$$

with: subscript i = number of line, superscript n = number of excitation, and superscript ν = number of mode.

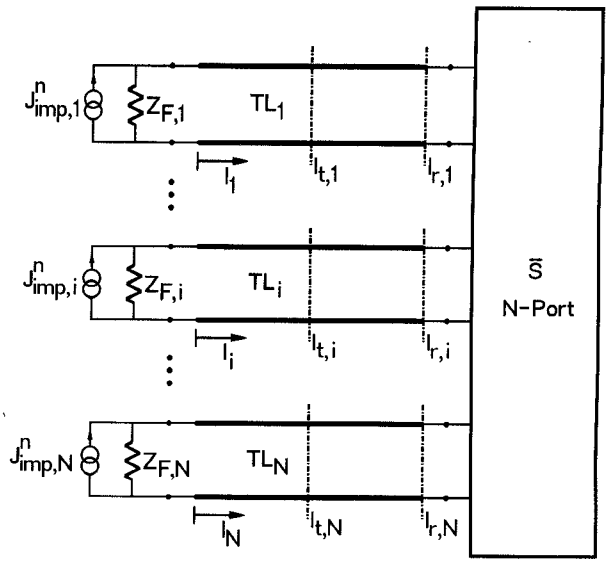

Fig. 5. Schematic representation of the excitation and extraction technique to derive N-port scattering parameters. n = number of excitation, i = number of port, ν = number of mode, $l_{t,i}$ = location of extraction plane, and $l_{r,i}$ = location of reference plane.

The next step is a test procedure described as

$$\iint_{A_{tr,i}} [\boldsymbol{E}^n_{tr,i} \times \boldsymbol{t}^\mu_{H,i}] \cdot \boldsymbol{n}_{l,i}\, dA = \sum_{\nu=1}^{M_i} \iint_{A_{tr,i}} [\boldsymbol{t}^\nu_{E,i} \times \boldsymbol{t}^\mu_{H,i}] \cdot \boldsymbol{n}_{l,i}\, dA \cdot \sqrt{Z^\nu_{F,i}}\, [a_i^{\nu,n} e^{-\gamma_i^\nu (l_{t,i} - l_{r,i})} + b_i^{\nu,n} e^{\gamma_i^\nu (l_{t,i} - l_{r,i})}], \quad (21)$$

$$\iint_{A_{tr,i}} [\boldsymbol{H}^n_{tr,i} \times \boldsymbol{t}^\mu_{E,i}] \cdot \boldsymbol{n}_{l,i}\, dA = \sum_{\nu=1}^{M_i} \iint_{A_{tr,i}} [\boldsymbol{t}^\nu_{H,i} \times \boldsymbol{t}^\mu_{E,i}] \cdot \boldsymbol{n}_{l,i}\, dA \cdot (\sqrt{Z^\nu_{F,i}})^{-1}\, [a_i^{\nu,n} e^{-\gamma_i^\nu (l_{t,i} - l_{r,i})} + b_i^{\nu,n} e^{\gamma_i^\nu (l_{t,i} - l_{r,i})}]. \quad (22)$$

The integrals in (21) and (22) can be calculated analytically in the direction perpendicular to the groundplane. Application of Parseval's theorem transforms the integration in the other direction into the spectral domain. Here efficient usage of FFT algorithms becomes possible again. The resulting equation system can be solved for the unknowns $a_i^{\nu,n}$ and $b_i^{\nu,n}$.

In general for an N-port problem, the procedure described above has to be repeated for N linear independent excitations in order to form a set of linear independent equations in the sense of

$$[\boldsymbol{b}^1, \cdots, \boldsymbol{b}^n, \cdots, \boldsymbol{b}^N] = \boldsymbol{S}[\boldsymbol{a}^1, \cdots, \boldsymbol{a}^n, \cdots, \boldsymbol{a}^N],$$
$$n = \text{Number of excitation}, \quad (23)$$

which can be solved for the unknown scattering matrix $\boldsymbol{S}$.

It is important to note that the modes which form a complete set of functions in the case of an infinitely long line, do not do so in (19) and (20) due to the influence of surface waves and radiation excited by the N-port structure. This is in general a problem in defining S-parameters in planar, open circuits. Because of the choice of a Galerkin test procedure in (21) and (22) the coefficients $a_i^{\nu,n}$ and $b_i^{\nu,n}$ are calculated in the sense of a least square approximation. This looks like the best possible choice.

III. Results

In the numerical results shown here, the considered microstrip discontinuities are printed on a 635 μm Al_2O_3 substrate ($\epsilon_r = 9.8$) with a conductor width of 625 μm or 635 μm. The characteristic impedance of such lines is approximately 50 Ω.

Fig. 6 shows the first structure under consideration. It is a simple test structure, an interconnection of two microstrip lines by a bond-wire. The gap width is $g = 635$ μm and the bridge height is $h = 200$ μm. The S-parameters of this structure are plotted in Fig. 7. The SDA results (symbols $\times$, $+$) are compared to those calculated with the finite-difference time-domain method [18] applied to exactly the same structure using two different discretizations. For the spectral domain calculation the width of the line is discretized with three elements. The first FDTD result (curves labeled with $FDTD_1$ in Fig. 7) is calculated with the same discretization. A good agreement between both methods, especially in the phase curves, is obtained. In the case of a discretization with nine elements for the FDTD-method (curves labeled with $FDTD_2$ in Fig. 7), the curves for the magnitudes show a better matching. This is due to the coarseness error included in the FDTD calculation [17]. The next figure (Fig. 8) illustrates the longitudinal component (y-directed) of the surface current density around the gap of the same structure for a frequency of $f = 10$ GHz. The current decreases to the end of the lines and goes up into the bond-wire structure.

In a next step, the influence of the bridge height and the gap width on the S-parameters of the same structure has been tested. These investigations are very similar to those in [1]. Fig. 9 shows the influence of the bridge height varying from $h = 25$ μm to $h = 250$ μm. As expected, the magnitude of the reflection coefficient S_{11} increases when increasing the bridge height. The next figure (Fig. 10) shows the influence of the gap width, varying from one time the strip width up to four times the strip width. Again the magnitude of the reflection coefficient S_{11} increases according to the gap width.

In order to compare the SDA results with measured results, a spiral inductor—layout in Fig. 11—has been built and measured. The spiral inductor contains two turns separated by a gap of width $s = 312.5$ μm. The connection was an air-bridge prefabricated of a circular wire with diameter 317.5 μm with a defined length of 4.0775 mm. For the numerical analysis, the vertical directed part of

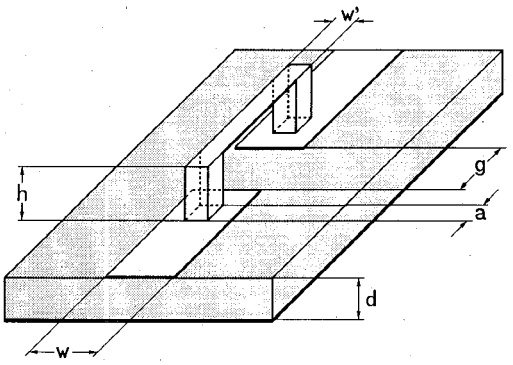

Fig. 6. Schematic view on the interconnection of two microstrip lines by a bond-wire, $\epsilon_r = 9.8$, $d = 635$ μm, $w = 635$ μm, $g = 635$ μm, $a = w' = 211.6$ μm, and $h = 200$ μm.

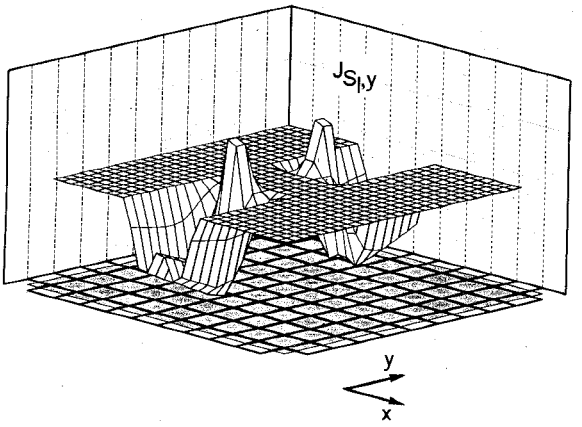

Fig. 8. Longitudinal current density around the bounded-gap-structure shown in Fig. 6. Frequency is 10 GHz.

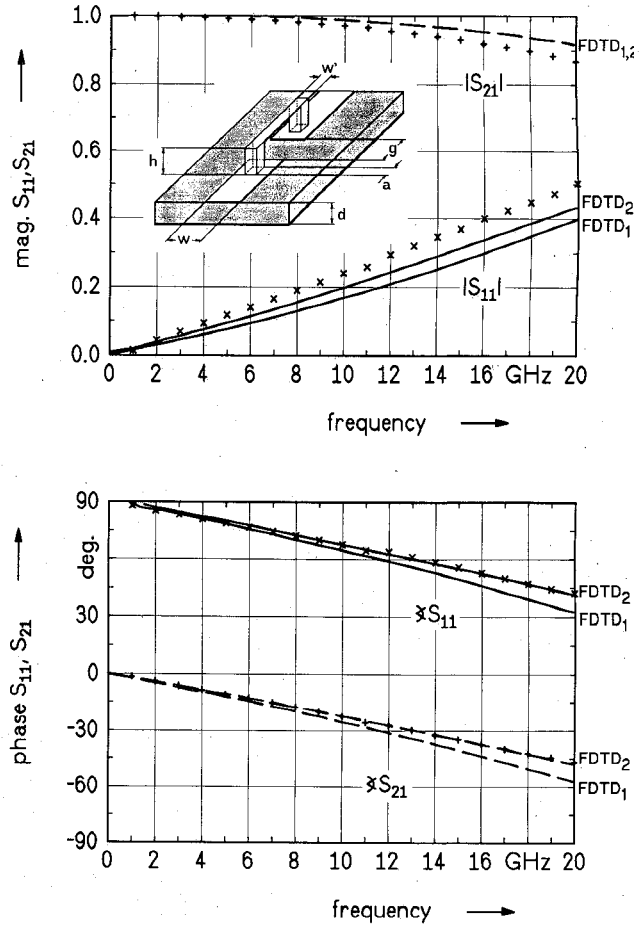

Fig. 7. S-parameters for the interconnection of two microstrip lines by a bond-wire. Geometry and material parameters as in Fig. 6 SDA results (symbols $\times$, $+$), FDTD results (lines ——, ---). Top: Magnitudes of S_{11}, S_{21}. Bottom: Phases of S_{11}, S_{21}.

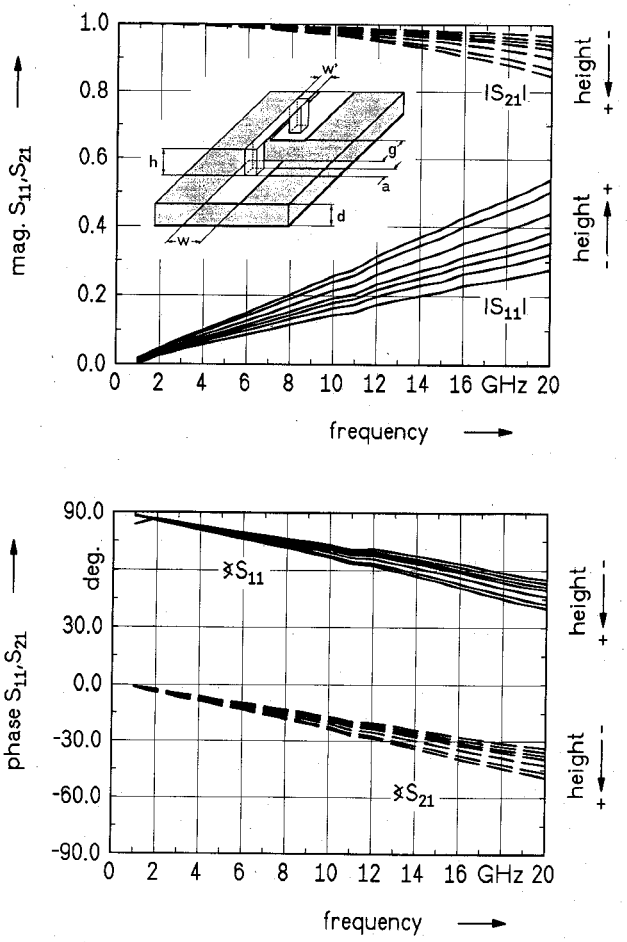

Fig. 9. S-parameters of the structure shown in Fig. 6 for different bridge heights, $h = 25, 50, 75, 100, 150, 200, 250$ μm. Top: Magnitudes of S_{11}, S_{21}. Bottom: Phases of S_{11}, S_{21}.

the bridge was modeled as a rectangular wire whereas the horizontal directed part was modeled as a flat strip (Fig. 11). The bridge height was $h = 317.5$ μm which was approximately the height of the lower edge of the horizontal part of the original circular wire. Impressed current source distributions and extraction planes have to be introduced

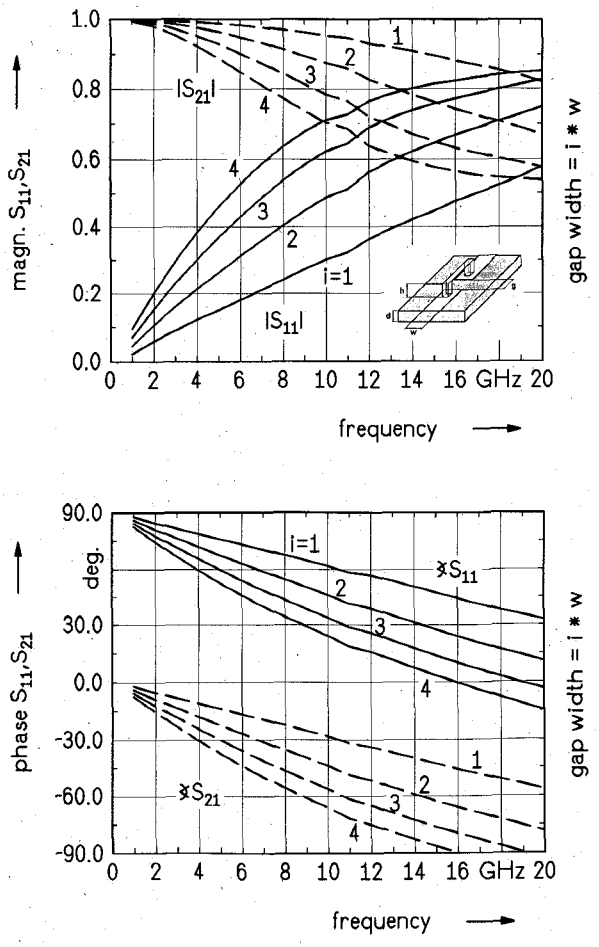

Fig. 10. S-parameters of the structure shown in Fig. 6 for different gap widths, $g = i \times w$, $i = 1, 2, 3, 4$. Top: Magnitudes of S_{11}, S_{21}. Bottom: Phases of S_{11}, S_{21}.

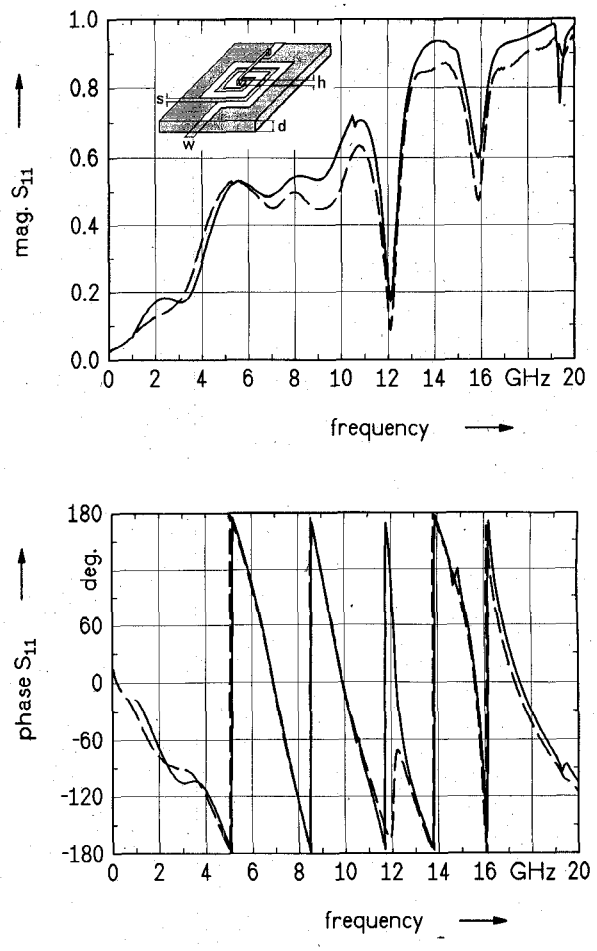

Fig. 12. Reflection coefficient S_{11} of the structure shown in Fig. 11. (———) calculated, (---) measured. Top: Magnitude of S_{11}. Bottom: Phase of S_{11}.

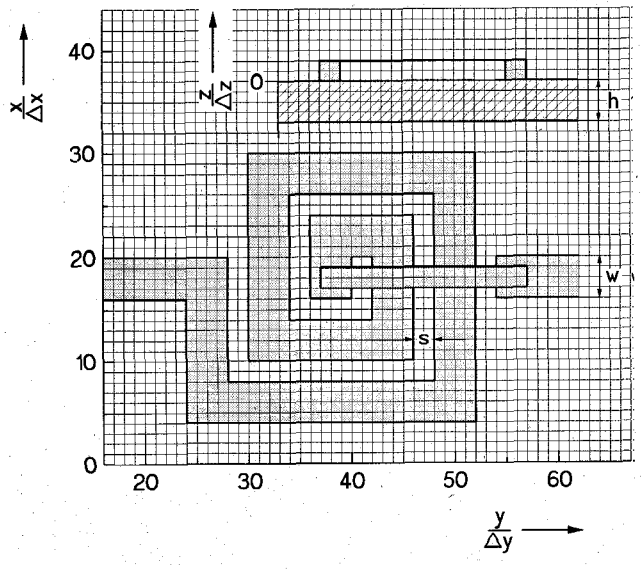

Fig. 11. Layout of the rectangular spiral inductor $\epsilon_r = 9.8$, $d = 635$ μm, $w = 625$ μm, $s = 312.5$ μm, $h = 317.5$ μm, $\Delta x = \Delta y = 156.25$ μm, and $\Delta z = 158.75$ μm.

for the calculation. The connected feeding lines at port 1 and port 2 have a length of 3.75 mm and 3.75 mm respectively. According to the Fig. 11, reference plane location of port 1 and 2 is at $y/\Delta y = 24$ and $y/\Delta y = 57$ respectively.

This structure was first introduced by [2]. The large geometrical dimensions have been chosen, because it was intended to have all the resonant phenomena of the component in a frequency range, that allows to verify the simulation by measurements. Smaller dimensions lead to higher resonant frequencies, but they don't influence the simulation and its accuracy. The strip width was discretized with four elements which results in a total number of $N_U = 1305$ unknowns. Figs. 12–14 demonstrate the excellent agreement of the analysis and measured results. Even the phase responses, which has been a critical aspect in nearly all other calculation methods, is predicted with a high accuracy by the SDA method. The calculated curves consist of nearly 300 frequency points. Figs. 15 and 16 illustrate the surface current density within two detailed areas of the spiral inductor at a frequency of

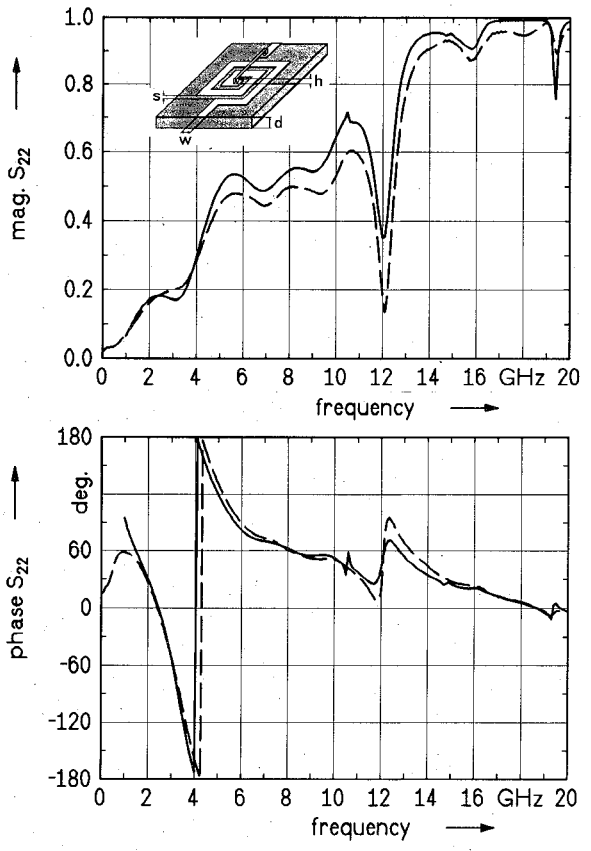

Fig. 13. Reflection coefficient S_{22} of the structure shown in Fig. 11. (———) calculated, (---) measured. Top: Magnitude of S_{22}. Bottom: Phase of S_{22}.

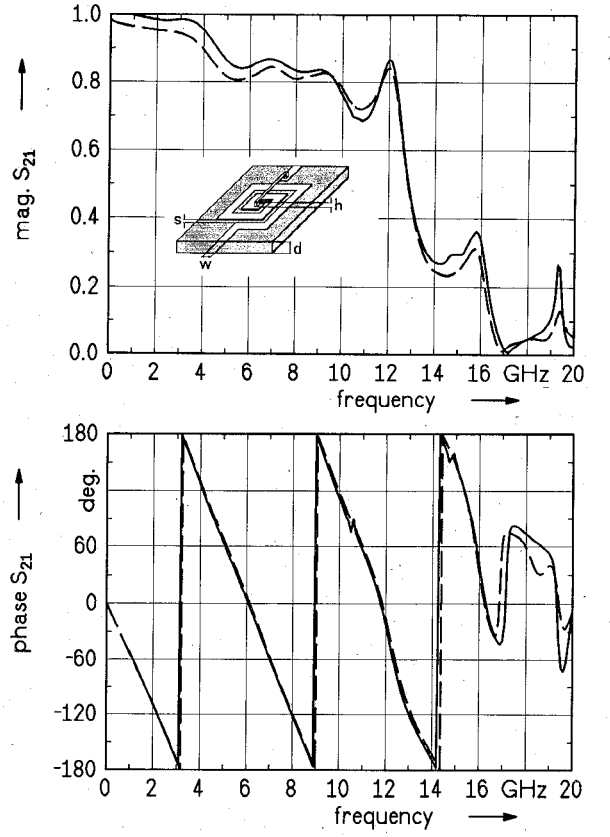

Fig. 14. Transmission coefficient S_{21} of the structure shown in Fig. 11. (———) calculated, (---) measured. Top: Magnitude of S_{21}. Bottom: Phase of S_{21}.

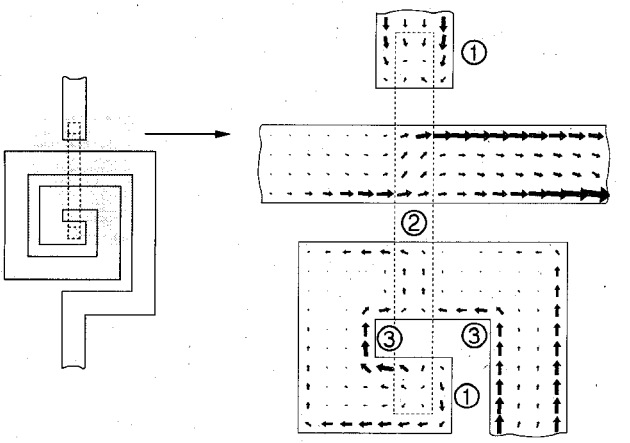

Fig. 15. Current distribution in the structure shown in Fig. 11 (f = 8.0 GHz). Detail 1.

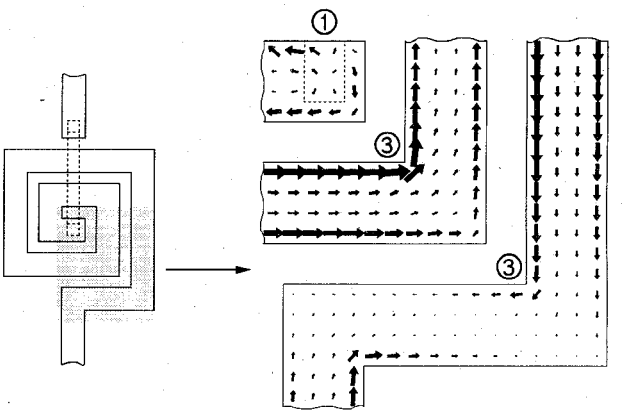

Fig. 16. Current distribution in the structure shown in Fig. 11 (f = 8.0 GHz). Detail 2.

f = 8 GHz. Some markers (1–3) have been introduced to draw attention to some remarkable details of the surface current flow. The marker 1 indicates the current flow from the planar metallization into the bond-wire structure. Next marker—marker 2—indicates disturbance of current flow on the lower metallization due to the influence of the upper part of the bridge 317.5 μm above. The current under the bridge, at a relative minimum for this frequency, changes from longitudinal direction nearly into pure lateral direction forced by the strong electromagnetic coupling to the air-bridge. The marker 3 points on some microstrip edges with typical current flow around the corner.

IV. Conclusion

In conclusion, the modified SDA method described here is a powerful tool to calculate 3D-microwave structures. It is possible to look for the influence of parameter variations as well as for coupling effects and losses due to non-ideal metallization or radiation within complex structures by application of this method. In connection with the S-parameter extraction technique described and with extensive use of FFT algorithm the method allows an efficient handling of 3D multiport problems. Even for complex structures, as the analyzed rectangular inductor, the method is very accurate compared to measurements.

REFERENCES

[1] A. Christ and H. L. Hartnagel, "Three-dimensional finite-difference method for the analysis of microwave-device embedding," *IEEE Trans. Microwave Theory Tech.*, vol. MTT-35, pp. 688–696, Aug. 1987.

[2] M. Rittweger and I. Wolff, "Analysis of complex passive (M)MIC-components using the finite-difference time-domain approach," in *1990 IEEE MTT-S Int. Microwave Symp. Dig.*, Dallas, 1990, pp. 1147–1150.

[3] W. J. R. Hoefer, "The transmission-line matrix method—theory and applications," *IEEE Trans. Microwave Theory Tech.*, vol. MTT-33, pp. 882–893, Oct. 1985.

[4] R. W. Jackson, "Full-wave, finite element analysis of irregular microstrip discontinuities," *IEEE Trans. Microwave Theory Tech.*, vol. 37, pp. 81–89, Jan. 1989.

[5] R. Brömme and R. H. Jansen, "Systematic investigation of coplanar waveguide MIC/MMIC structures using a unified strip/slot 3D electromagnetic simulator," in *1991 IEEE MTT-S Int. Microwave Symp. Dig.*, Boston, 1991, pp. 1081–1084.

[6] N. I. Dib, P. B. Katehi, and G. E. Ponchak, "Analysis of shielded CPW discontinuities with air-bridges," in *1991 IEEE MTT-S Int. Microwave Symp. Dig.*, Boston, pp. 469–472.

[7] A. Skriverik and J. R. Mosig, "Equivalent circuits of microstrip discontinuities including radiation effects," in *1989 IEEE MTT-S Dig.*, Long Beach, 1989, pp. 1147–1150.

[8] T. Becks, G. Gronau, and I. Wolff, "Efficient S-parameter calculation of multiport planar structures with the spectral domain analysis method," in *1991 IEEE MTT-S Int. Microwave Symp. Dig.*, Boston, 1991, pp. 353–356.

[9] T. Becks and I. Wolff, "Calculation of three-dimensional passive structures including bond-wires, via-holes and air-bridges using the spectral domain analysis method," in *21th European Microwave Conf. Proc.*, Stuttgart, 1991, pp. 571–576.

[10] N. K. Das and D. M. Pozar, "A generalized spectral-domain Green's function for multilayer dielectric substrates with application to multilayer transmission lines," *IEEE Trans. Microwave Theory Tech.*, vol. MTT-35, pp. 326–335, Mar. 1987.

[11] T. Dolny, "Berechnung der elektromagnetischen Felder einer Einheitsanregung in geschichteten, planaren Wellenleitern," Diploma-Thesis, Duisburg University, 1990.

[12] T. Becks and I. Wolff, "Improvements of spectral domain analysis techniques for arbitrary planar circuits," in *Directions in Electromagnetic Modeling*, H. L. Bertoni and L. B. Felsen, Eds. New York: Plenum, 1991, pp. 339–346.

[13] W. Wertgen and R. H. Jansen, "A 3D field-theoretical simulation tool for the CAD of mm-wave MMIC's," *Alta Frequenca*, vol. LVII, no. 5, pp. 203–216, June 1988.

[14] R. Chandra, "Conjugate gradient methods for partial differential equations," Ph.D. dissertation, Yale University, New Haven, CT, 1978.

[15] H. Simon, "The Lanczos algorithm for solving symmetric linear systems," Ph.D. dissertation, University of California, Berkeley, 1982.

[16] H. L. Nyo and R. F. Harrington, "The discrete convolution method for solving some large moment matrix equations," Tech. Rep. No. 21, Department of Electrical and Computer Engineering, Syracuse University, Syracuse, NY, July 1983.

[17] C. J. Railton and J. P. McGeehan, "Analysis of microstrip discontinuities using the finite difference time domain technique," in *1989 IEEE MTT-S Int. Microwave Symp. Dig.*, Long Beach, CA, 1989, pp. 997–1000.

[18] M. Rittweger, private communication.

Thomas Becks received the Dipl.-Ing. degree in electrical engineering in 1988 from Duisburg University, Duisburg, Germany.

Since 1988 he has been with the Department of Electrical Engineering and Sonderforschungsbereich 254, Duisburg University. He is currently working towards the Dr.-Ing. degree. His research interests are in the area of electromagnetic simulations of microwave and millimeter-wave passive components.

Ingo Wolff (M'75–SM'85–F'88) was born in Köslin, Germany, in 1938. He received the Dipl.-Ing., doctoral, and habilitation degrees in 1964, 1967, and 1970, respectively, all from the Technical University of Aachen, Germany.

From 1970 to 1974 he was a Lecturer and Associate Professor for high-frequency techniques in Aachen. Since 1974 he has been a Full Professor of Electromagnetic Field Theory at the Duisburg University, Duisburg, Germany. His main areas of research are electromagnetic field theory applied to the computer-aided design of MIC's and MMIC's, millimeter-wave components and circuits, and the field theory of anisotropic materials.